Check for updates

High-pressure synthesis and magnetic properties of tetragonal R_2BaCuO_5 (R = Sm and Eu)

Swarnamayee Mishra[1], Premakumar Yanda[1], Shrikant Bhat[2], Martin Etter[2] and A. Sundaresan[1]*

[1]Chemistry and Physics of Materials Unit, Jawaharlal Nehru Centre for Advanced Scientific Research, School of Advanced Materials, Bangalore, India, [2]Deutsches Elektronen-Synchrotron (DESY), Hamburg, Germany

We report the experimental discovery of a new structural phase of well-known orthorhombic R_2BaCuO_5 (R = Sm and Eu), exhibiting a tetragonal crystal structure with space group $P4/mbm$. The high-pressure tetragonal phase is isostructural with the brown phase R_2BaCuO_5 (R = La, Pr, and Nd). In this structure, the Cu ions form an isolated square planar environment, contrary to the orthorhombic phase, where the Cu ions are located in a distorted square pyramid. Magnetization and specific heat measurements reveal the long-range antiferromagnetic order of the Cu^{2+} and/or Sm^{3+} moments for the Sm-sample, with the magnetic specific heat accounting for only 35% of the magnetic entropy. Interestingly, the Eu-sample remains paramagnetic down to the lowest temperature. The high Curie-Weiss temperature of −140 K and magnetic entropy of 3% of the expected value indicates that the system is highly frustrated. We estimated the isothermal entropy change and investigated the magnetocaloric effect for Eu_2BaCuO_5, and the maximum entropy change detected at a field of 70 kOe at 3 K reaches 5.6 J $kg^{-1}K^{-1}$.

KEYWORDS

high-pressure synthesis, polymorphism, antiferromagnetism, magnetocaloric effect, paramagnetism

1 Introduction

The oxides of the general formula R_2BaMO_5 (R = rare-earth, M = 3d-transition metal) form a large family of compounds that crystallize into four different structural types with intriguing magnetic properties (Michel and Raveau, 1982; 1983 St. Schiffler and Müller-Buschaum, 1986; St. Schiffler and Müller-Buschbaum, 1986; 1987a; 1987b; Mevs and Müller-Buschbaum, 1989; Mevs and Müller-Buschbaum, 1989; Müller-Buschbaum and Sonne, 1990; Amador et al., 1990; Salinas-Sánchez, Sáez-Puche, and Alario-Franco, 1990; Salinas-Sánchez et al., 1991; Sáez-Puche et al., 1992; Salinas-Sánchez et al., 1992; García-Matres, Martínez, et al., 1993; De Andrés et al., 1993; Sáez-Puche and Hernández-Velasco, 1994; Hernández-Velasco, Salinas-Sánchez, and Sáez-Puche, 1994). Amongst these, the best known is the green phase R_2BaCuO_5 (R = Sm-Gd, Dy-Lu, Y) compounds exhibiting the orthorhombic structure with space group $Pnma$ where the coordination polyhedron of copper is a distorted tetragonal pyramid CuO_5 which is linked by monocapped trigonal prisms (RO_7) by sharing triangular faces. In this structure, the Ba^{2+} ions are coordinated with eleven oxygen atoms forming an irregular BaO_{11} polyhedron. This structure is shown by most of the copper and some of the nickel, cobalt, and zinc oxides. The second kind, Nd_2BaPtO_5, is a tetragonal structure with space group $P4/mbm$ with the Pt atoms located at

TABLE 1 Comparison of magnetic properties among R_2BaCuO_5 (R = rare-earth cations) compounds. FM and AFM mean ferromagnetic and antiferromagnetic orderings, respectively.

Compound	Structure type	Magnetic ordering type	Magnetic ordering temperature (K)		Reference
			T_N^{Cu}/T_C^{Cu}	T_N^R	
La_2BaCuO_5	$P4/mbm$	FM	5.7	-	Salinas-Sánchez and Sáez-Puche, 1993
Pr_2BaCuO_5	$P4/mbm$	AFM	20		Sáez-Puche, Herrera, and Martínez 1998; Puche et al., 2008
Nd_2BaCuO_5	$P4/mbm$	AFM	7.8		Sáez Puche et al., 2006
Sm_2BaCuO_5	$Pnma$	AFM	23	5	Levitin et al., 1990
Eu_2BaCuO_5	$Pnma$	AFM	16	-	Levitin et al., 1990
Gd_2BaCuO_5	$Pnma$	AFM	11.9		Levitin et al., 1990
Dy_2BaCuO_5	$Pnma$	AFM	18	10	Levitin et al., 1990; Salinas-Sánchez, Sáez-Puche, and Alario-Franco 1990
Ho_2BaCuO_5	$Pnma$	AFM	17	8	Levitin et al., 1990
Er_2BaCuO_5	$Pnma$	AFM	19	5	Levitin et al., 1990
Tm_2BaCuO_5	$Pnma$	AFM	19	-	Levitin et al., 1990
Yb_2BaCuO_5	$Pnma$	AFM	16	<2	Levitin et al., 1990
Lu_2BaCuO_5	$Pnma$	AFM	19	-	Levitin et al., 1990
Y_2BaCuO_5	$Pnma$	AFM	28	-	Chattopadhyay et al., 1989

an isolated square planar environment PtO_4, forming a quasi-bi-dimensional arrangement. The third kind, R_2BaZnO_5 (R = La and Nd), is a tetragonal $I4/mcm$ structure where Zn^{2+} ions are in tetrahedral coordination. The fourth one is the so-called Nd_2BaNiO_5 structure type showing orthorhombic symmetry with space group $Immm$. This structure can be described by isolated chains of corner-shared (NiO_6) octahedra running parallel to the a-axis, giving rise to a one-dimensional character. In addition, there exists a dimorphism for R_2BaMO_5 (M = Ni and Co) with smaller size R-ion, which crystallize in both $Pnma$ and $Immm$ structures depending on the synthesis conditions (Salinas-Sánchez et al., 1991; García-Matres, Rodríguez-Carvajal, et al., 1993; Hernández-Velasco and Sáez-Puche, 1993).

The R_2BaCuO_5 oxides have two different structures depending on the lanthanide trivalent cation size. For lanthanide ions Sm-Gd, Dy-Lu and Y, the structure is orthorhombic with space group $Pnma$, called the "green phase". Whereas a tetragonal structure of cuprates, the so-called "brown phase" is observed for R = La, Pr, and Nd, space group $P4/mbm$. Table 1 shows a comparison of structural types, magnetic properties, and the ordering temperatures among R_2BaCuO_5 compounds. It can be noted that previous studies reveal some of the green phase compounds exhibited strong magnetoelectric coupling, mainly due to the interplay of $4f$-$3d$ magnetic interactions (Indra et al., 2019; Yanda, Ter-Oganessian, and Sundaresan, 2019; Yanda et al., 2020; 2021). For example,

Sm_2BaCuO_5 demonstrates a linear magnetoelectric effect below the Cu^{2+} spins ordering temperature, and this coupling is further affected by the Sm^{3+} spins ordering (Indra et al., 2019; Yanda, Ter-Oganessian, and Sundaresan, 2019). Also, Gd_2BaCuO_5 is shown to exhibit multiferroic properties (Yanda et al., 2020). Further, Dy_2BaCuO_5 and Ho_2BaCuO_5 compounds evidence the linear magnetoelectric effect and field-induced multiferroicity, while Er_2BaCuO_5 exhibits field-induced electric polarization around 5.1 K above the critical field $H_c \sim 0.9$ T, indicating coupling between magnetism and electric polarization (Indra et al., 2019; Yanda et al., 2021). The remaining compounds in the green phase series with R = Eu, Y, Tm, and Lu, however, do not show magnetoelectric coupling (Yanda, 2021).

Recently, three new members of the R_2BaZnO_5 for R = Pr, Sm, and Eu were synthesized by a high-pressure and high-temperature method indicating polymorphism for Sm- and Eu- crystallizing in both $Pnma$ and $I4/mcm$ (Ishii et al., 2020). Considering the structural phase transition from orthorhombic to tetragonal for R_2BaZnO_5 and the different cation coordination in both phases, it will be interesting to study the evolution of the crystal structure of the R_2BaCuO_5 family under pressure. Also, if it shows polymorphism, different magnetic properties can be expected for R_2BaCuO_5. Herein, we report the stabilization of the tetragonal phase of R_2BaCuO_5 (R = Sm and Eu) under high-pressure and high-temperature and their crystal structure and magnetic properties.
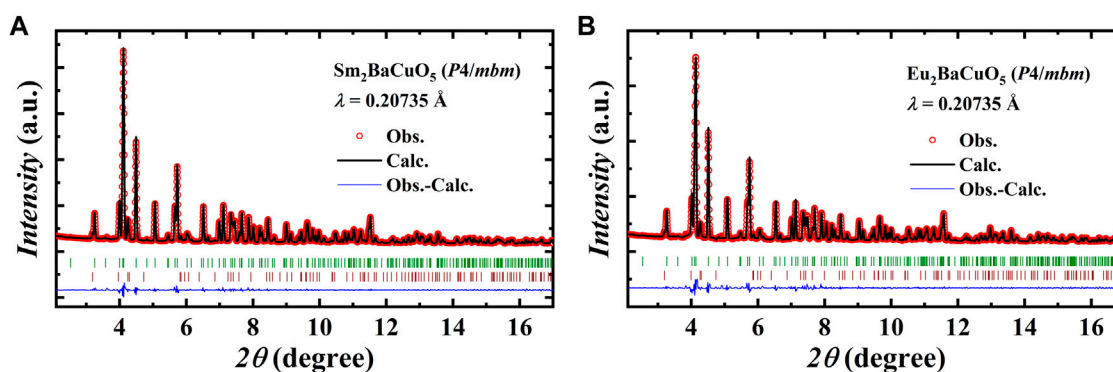
FIGURE 1
Rietveld refined synchrotron XRD pattern collected at RT of **(A).** Sm_2BaCuO_5 and **(B).** Eu_2BaCuO_5 in tetragonal phase, respectively. The second row of vertical tick marks indicates the secondary phase R_2CuO_4 (R = Sm and Eu).

TABLE 2 Structural parameters obtained from Rietveld refinement of room temperature powder synchrotron XRD pattern of Sm_2BaCuO_5 in space group $P4/mbm$. $a = b = 6.6355$ (3) Å, $c = 5.7993$ (3) Å, $\alpha = \beta = \gamma = 90$ °, $V = 255.34$ (2) Å³; and the goodness of the fit $\chi^2 = 2.45$; $R_p = 1.79$ (%), $R_{wp} = 2.73$ (%).

Atom	Wyckoff position	Symmetry	x	y	z	B_{iso} (Å²)	Occ
Sm	$4h$	$m.2m$	0.1737 (2)	0.6737 (2)	0.5000	0.52 (4)	1
Ba	$2a$	$4/m..$	0.0000	0.0000	0.0000	0.50 (5)	1
Cu	$2d$	$m.mm$	0.0000	0.5000	0.0000	0.73 (9)	1
O1	$2b$	$4/m..$	0.0000	0.0000	0.5000	0.61 (23)	1
O2	$8k$	$..m$	0.3607 (15)	0.8607 (15)	0.7611 (16)	0.35 (23)	1

2 Experimental section

Polycrystalline samples of orthorhombic R_2BaCuO_5 (R = Sm and Eu) were prepared as starting materials by the conventional solid-state synthesis procedure starting from the stoichiometric mixture of high-purity R_2O_3, $BaCO_3$, and CuO. The reactants were ground, followed by thermal treatments at 1,000°C in the air for 12 h with some intermediate grindings to homogenize the reaction products. Two different high-pressure machines were used to prepare and study the tetragonal phases. In the first step, the samples were treated with a pressure of 4.5 GPa and a temperature of 1,000°C in a laboratory-based cubic multi-anvil high-pressure apparatus. This transformed the R_2BaCuO_5 (R = Sm and Eu) to the tetragonal phase, which was characterized by powder x-ray diffraction at the powder diffraction and total scattering beamline P02.1 (PETRA III at DESY, Hamburg, Germany), with the wavelength of 0.20735 Å (Dippel et al., 2015). The sample detector distance (SDD) for XRD experiments was set to ~1,000 mm. In the second step, *in situ* energy-dispersive x-ray diffraction spectra (EDXRD) at different pressure and temperature conditions were collected for orthorhombic Sm_2BaCuO_5. This experiment was performed in a Hall-type six-ram LVP (mavo press LPQ6 1,500–100; Max Voggenreiter GmbH, Germany) installed at the P61B beamline at DESY, Hamburg (Farla et al., 2022) using DESY standard 14/7 high-pressure assembly. Cr_2O_3-doped MgO octahedron was used as a pressure transmitting medium along with a tubular-resistive graphite heater. The pressure exerted at different press loads on the sample was

calculated from *in situ* EDXRD data (using a MgO pressure marker) and temperature values were deduced from the Power-Temperature relationship (at the corresponding press load). The recovered sample was then characterized by a PANalytical Empyrean alpha-1 diffractometer using monochromatized Cu Kα1 radiation (λ = 1.5406 Å). The XRD pattern of all the samples was qualitatively analyzed by the Rietveld method using the program FULLPROF suite (Rodríguez-Carvajal, 1993). EDXRD profiles were analyzed using the PDIndexer software package provided by Seto Y (Seto et al., 2010; Seto, 2012). DC magnetization measurements were performed using a superconducting quantum interference device (SQUID) magnetometer (MPMS, Quantum Design). Specific heat capacity (C_p) measurement was performed in the physical property measurement system (PPMS, Quantum Design) that provides temperature control and an external magnetic field.

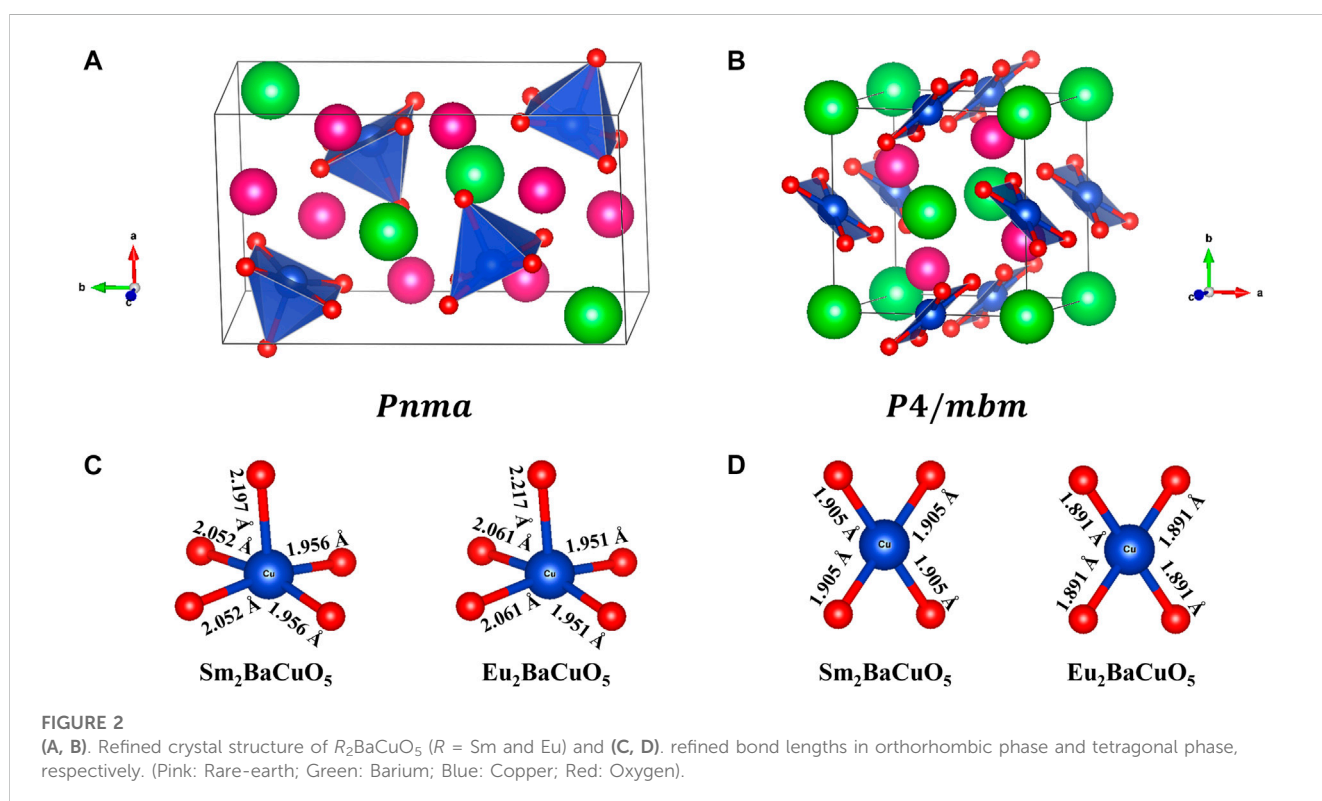# 3 Results and discussion

3.1 Crystal structure

Analysis of the room temperature XRD pattern of ambient pressure R_2BaCuO_5 (R = Sm and Eu) precursor, prepared by conventional solid-state synthesis, confirms an orthorhombic phase (space group *Pnma*), as illustrated in Supplementary Figure S1. The corresponding refined structural parameters are given in Supplementary Tables S1, S2,

TABLE 3 Structural parameters obtained from Rietveld analysis of room temperature powder synchrotron XRD pattern of Eu_2BaCuO_5 in space group $P4/mbm$. $a = b = 6.6052\,(4)$ Å, $c = 5.7900\,(4)$ Å, $\alpha = \beta = \gamma = 90\,°$, V = 252.61 (3) Å³; and the goodness of the fit $\chi^2 = 3.93$; $R_p = 2.38$ (%), $R_{wp} = 3.55$ (%).

Atom	Wyckoff position	Symmetry	x	y	z	B_{iso} (Å²)	Occ
Eu	$4h$	$m.2m$	0.1736 (2)	0.6736 (2)	0.5000	0.55 (4)	1
Ba	$2a$	$4/m..$	0.0000	0.0000	0.0000	0.36 (7)	1
Cu	$2d$	$m.mm$	0.0000	0.5000	0.0000	0.61 (12)	1
O1	$2b$	$4/m..$	0.0000	0.0000	0.5000	0.72 (33)	1
O2	$8k$	$..m$	0.3603 (22)	0.8603 (22)	0.7637 (22)	0.60 (33)	1

FIGURE 2
(A, B). Refined crystal structure of R_2BaCuO_5 (R = Sm and Eu) and (C, D). refined bond lengths in orthorhombic phase and tetragonal phase, respectively. (Pink: Rare-earth; Green: Barium; Blue: Copper; Red: Oxygen).

which are in good agreement with the values obtained in the literature (Michel and Raveau, 1982; Salinas-Sánchez et al., 1992). The orthorhombic R_2BaCuO_5 (R = Sm and Eu) were subjected to high-pressure and high-temperature (HP-HT) conditions (4.5 GPa and 1,000°C). The XRD pattern of the HP-HT products obtained at the powder diffraction and total scattering beamline P02.1, with the wavelength of 0.20735 Å, is shown in Figure 1. We tried to index the data with the orthorhombic (SG: $Pnma$ and $Immm$), tetragonal (SG: $P4/mbm$ and $I4/mcm$) models, reported for R_2BaMO_5. The tetragonal model (SG: $P4/mbm$) yielded a reliable solution consistent with the structure reported for R_2BaCuO_5 (R = La, Pr, and Nd).

Derived atomic positions and other structural parameters of both Sm_2BaCuO_5 and Eu_2BaCuO_5 in the tetragonal $P4/mbm$ phase are shown in Table 2, 3, respectively. In the tetragonal phase, a small amount of Sm_2CuO_4 and Eu_2CuO_4 impurities

coexist with the primary phase of Sm- and Eu- samples, respectively. In the $Pnma$ polymorph, the rare-earth atoms are in two different crystallographic sites (Michel and Raveau, 1982; Salinas-Sánchez et al., 1992), whereas they occupy only one site in the case of $P4/mbm$. As shown in Figures 2A, B, the coordination environments of the $3d$ copper atom change from CuO_5 in the $Pnma$-structure to CuO_4 square planar for the $P4/mbm$-phase.

Further, the bond lengths for the copper polyhedra in both forms are shown in Figures 2C, D. From this, it is clear that the square pyramid CuO_5 shows strong distortion compared to square planar CuO_4, which has zero distortion because of its regular shape. The distortion parameter obtained for CuO_5 calculated with the formula

$$\nabla d = \frac{1}{n} \sum_n \left[\frac{d_n - d_{av}}{d_{av}} \right]^2 \qquad (1)$$
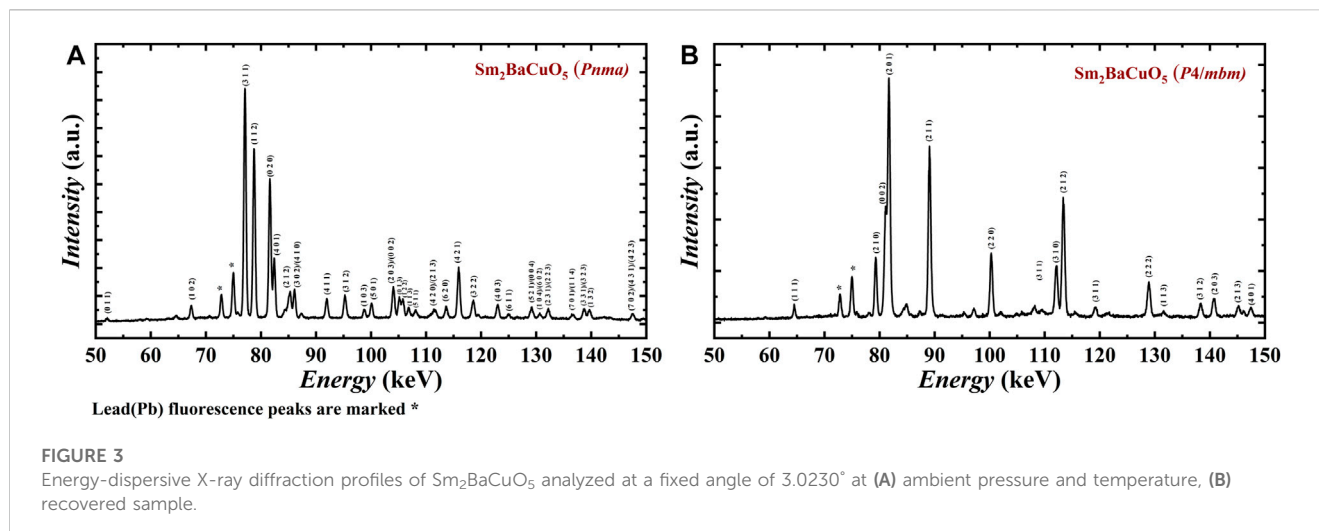
FIGURE 3
Energy-dispersive X-ray diffraction profiles of Sm$_2$BaCuO$_5$ analyzed at a fixed angle of 3.0230° at **(A)** ambient pressure and temperature, **(B)** recovered sample.

TABLE 4 Structural parameters obtained from Rietveld refinement of room temperature powder XRD pattern of Sm$_2$BaCuO$_5$ (10.9 GPa and 823 °C) in space group *P4/mbm*. $a = b = 6.6277$ (1) Å, $c = 5.7936$ (1) Å, $\alpha = \beta = \gamma = 90$ °, V = 254.49 (1) Å³; and the goodness of the fit $\chi^2 = 1.55$; $R_P = 3.50$ (%), $R_{wp} = 4.60$ (%).
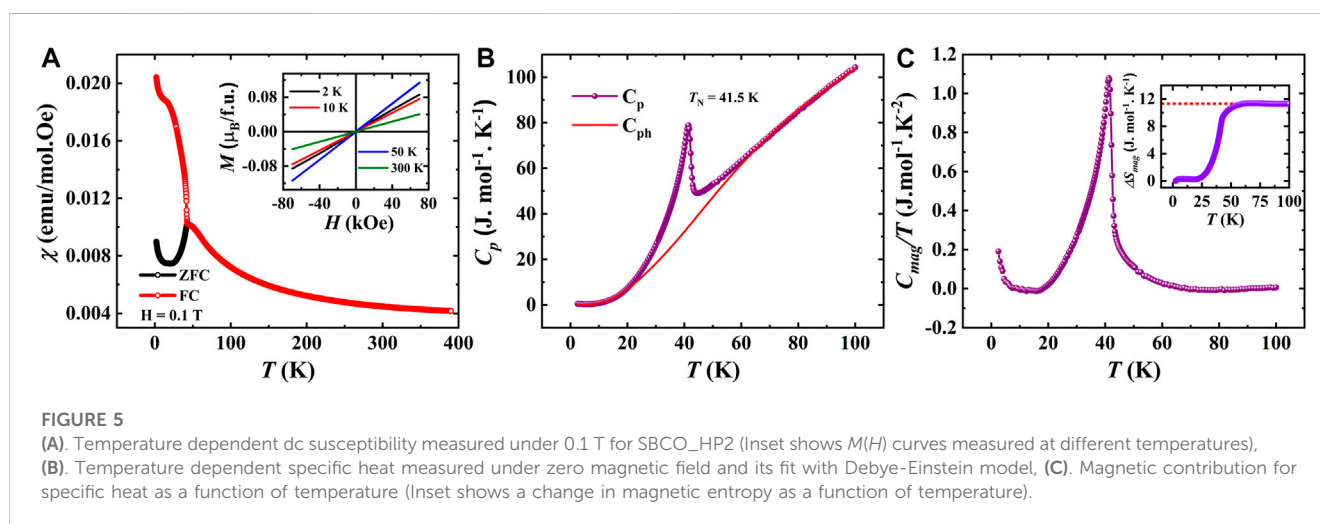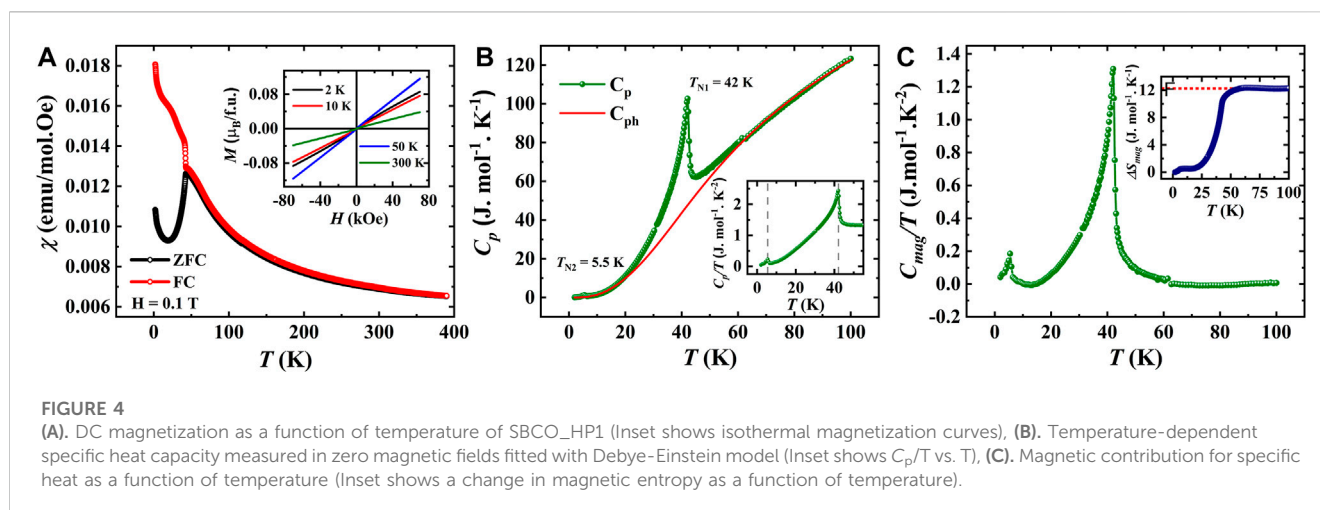
Atom	Wyckoff position	Symmetry	x	y	z	B_{iso} (Å²)	Occ
Sm	4h	m.2m	0.1734 (2)	0.6734 (2)	0.5000	0.36 (5)	1
Ba	2a	4/m..	0.0000	0.0000	0.0000	0.37 (8)	1
Cu	2d	m.mm	0.0000	0.5000	0.0000	0.32 (16)	1
O1	2b	4/m..	0.0000	0.0000	0.5000	1.000	1
O2	8k	..m	0.3568 (21)	0.8607 (21)	0.7660 (27)	1.000	1

are 1.9×10^{-3} and 2.3×10^{-3}, for Sm- and Eu- samples, respectively, where d_n and d_{av} are individual and average metal-oxygen bond lengths and n is the number of bonds in the polyhedra.

To investigate this high-pressure structural evolution, Sm$_2$BaCuO$_5$ in the orthorhombic phase was probed using energy dispersive x-ray diffraction (EDXRD), using a synchrotron white beam when the sample was exposed to different P-T conditions. The diffracted x-rays are energy analyzed at a fixed angle of 3.0230° in a continuous energy range of 30–160 keV. The obtained EDXRD spectra of Sm$_2$BaCuO$_5$ under ambient conditions are shown in Figure 3A, and the spectrum is consistent with the orthorhombic phase, indexed by the PDIndexer software. The sample was then subjected to pressure, and the corresponding *in situ* XRD patterns are shown in Supplementary Figure S2A. Upon compression, we observed the broadening of all reflections, and we could only detect 3–4 major broad reflections above a pressure of 1 GPa. These can be related to pressure-induced effects (amorphization or disorder state) on the sample. This effect remains consistent throughout the pressure range of 1–10.9 GPa, along with the pressure effect (peak shift). The swift change of spectra above 1 GPa also suggests the possible reorganization or disordering happens at a very early stage of the compression. On heating, reflections are getting sharper (a sign of order/recrystallization) again. The corresponding *in situ*

spectra obtained at 10.9 GPa, and various temperatures are shown in Supplementary Figure S2B. It shows that the tetragonal phase appears around 720°C at 10.9 GPa. This also suggests that the orthorhombic phase transforms into disordered/amorphous state upon compression, then directly converts to a tetragonal phase upon heating. The tetragonal phase obtained at 10.9 GPa and 823°C could be retained after the quenching and recovered after decompression. The corresponding spectra are shown in Figure 3B. The sample was then crushed and measured by the laboratory angle-resolved x-ray diffraction to perform a conventional Rietveld refinement. The obtained structural parameters are enlisted in Table 4, which agrees well with the phase obtained at 4.5 GPa and 1,000°C in our high-pressure apparatus. It can be noted that at 10.9 GPa, the transition is completed within a few minutes and well below 1,000°C. We speculate that the observed phase transformation of Sm$_2$BaCuO$_5$ from orthorhombic to a tetragonal structure may be possible just above 1 GPa and at temperatures above 1,000°C. It is also to be noted that the tetragonal phase is stable till 10.9 GPa, supported by *in situ* experiments.

For physical property measurements, to avoid confusion for the readers, we have now named the tetragonal structured Sm$_2$BaCuO$_5$ and Eu$_2$BaCuO$_5$ synthesized at 4.5 GPa and 1,000°C in a cubic multi-anvil high-pressure apparatus installed at our lab as SBCO_

FIGURE 4
(A). DC magnetization as a function of temperature of SBCO_HP1 (Inset shows isothermal magnetization curves), **(B).** Temperature-dependent specific heat capacity measured in zero magnetic fields fitted with Debye-Einstein model (Inset shows C_p/T vs. T), **(C).** Magnetic contribution for specific heat as a function of temperature (Inset shows a change in magnetic entropy as a function of temperature).

FIGURE 5
(A). Temperature dependent dc susceptibility measured under 0.1 T for SBCO_HP2 (Inset shows $M(H)$ curves measured at different temperatures), **(B).** Temperature dependent specific heat measured under zero magnetic field and its fit with Debye-Einstein model, **(C).** Magnetic contribution for specific heat as a function of temperature (Inset shows a change in magnetic entropy as a function of temperature).

HP1, EBCO_HP and the recovered Sm_2BaCuO_5 sample obtained at 10.9 GPa and 823°C as SBCO_HP2 in an LVP installed at the P61B beamline at DESY.

3.2 Magnetic properties

The temperature dependence of dc magnetic susceptibility $\chi(T)$ in an applied magnetic field of 0.1 T under both zero field-cooled (ZFC) and field-cooled (FC) procedures for SBCO_HP1 sample is presented in Figure 4A, which evidence a spontaneous change in $\chi(T)$ near 42 K and a small change near 5.5 K, indicating that the compound undergoes two successive magnetic transitions. Further information on the nature of the magnetic state is obtained from magnetic field-dependent magnetization, which was measured at four different temperatures (2, 10, 50, and 300 K), and the results are presented in the inset of Figure 4A. At 300 K, the magnetization is linear up to magnetic fields of 7 T,

consistent with the paramagnetic nature. Also, the linear behavior of magnetization curves measured below 42 K, namely, at 2 and 10 K in the entire field regime, confirm the antiferromagnetic character of the compound. A splitting between ZFC and FC susceptibility branches was observed just below 42 K, which is a possible indication of the occurrence of a glassy-like magnetic behavior. Therefore, we carried out the ac magnetic susceptibility measurements on the SBCO_HP1 sample to examine the dynamic effects linked to magnetically frustrated properties and examine whether the susceptibility anomaly is associated with a glass behavior. The in-phase component M′ and the out-of-phase component M″ of the complex ac magnetization with varying frequencies are shown in Supplementary Figure S3. A sharp transition is noticed around 42 K, which agrees with the dc magnetic measurements. And this maximum has no dependence on the applied ac magnetic field frequency. It confirms that the ZFC-FC bifurcation at 42 K is not associated with the spin-glass transition and confirms the
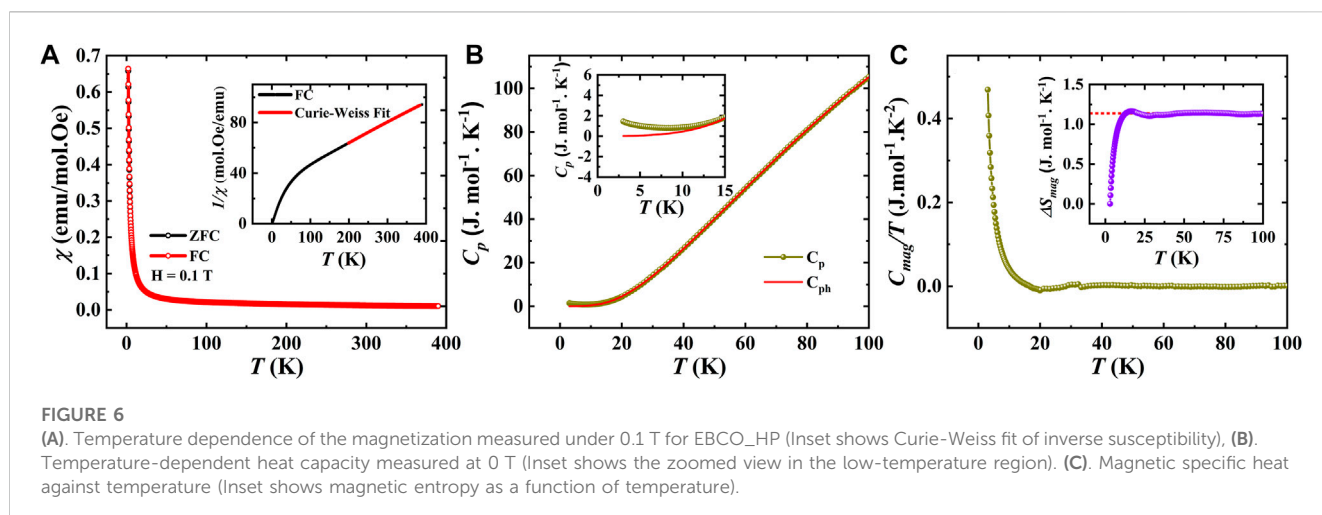
FIGURE 6
(A). Temperature dependence of the magnetization measured under 0.1 T for EBCO_HP (Inset shows Curie-Weiss fit of inverse susceptibility), **(B)**. Temperature-dependent heat capacity measured at 0 T (Inset shows the zoomed view in the low-temperature region). **(C)**. Magnetic specific heat against temperature (Inset shows magnetic entropy as a function of temperature).

long-range magnetic ordering. However, we did not observe any features in the imaginary part.

Further, to investigate the antiferromagnetic transitions, heat capacity measurements have been carried out under zero applied magnetic field. The λ-type transitions at 42 and 5.5 K, as displayed in Figure 4B, confirm two long-range magnetic orderings. However, neutron diffraction studies are required to verify the Cu^{2+} and/or Sm^{3+} ion orderings. In order to assess the magnetic entropy changes, the phononic contribution to the specific heat has been estimated by fitting the heat capacity using the Debye-Einstein model, as shown in Figure 4B. The magnetic specific heat is obtained by subtracting C_{ph} from C_p, and its temperature variation is shown in Figure 4C. The magnetic entropy is further obtained by integrating the magnetic specific heat C_{mag}/T, which yields the magnetic entropy changes 12.3 J mol^{-1}K^{-1}. The obtained entropy is 35% of the theoretically predicted value of $R[ln(S_{Sm}+1)^2(S_{Cu}+1)] = 35.6$ J mol^{-1}K^{-1} for $S_{Sm} = \frac{5}{2}$ and $S_{Cu} = \frac{1}{2}$ spins, which suggests the presence of strong magnetic frustration present in the sample.

The temperature-dependent magnetic susceptibility $\chi(T)$ in both ZFC and FC modes investigated on the SBCO_HP2 sample are shown in Figure 5A. In contrast to SBCO_HP1, these curves suggest a single AFM transition with T_N of about 41.5 K, which is supported by the heat capacity curve as displayed in Figure 5B. Subsequent isothermal magnetization curves, M(H), at 2 K, 10 K, 50 K, and 300 K, are given in the inset of Figure 5A. The curves below T_N are linear and in good agreement with the antiferromagnetic ordering of Cu- and Sm-ions and room temperature data resembling the paramagnetic behavior. Further, we have fitted the heat capacity with the Debye-Einstein model, as shown in Figure 5B, to calculate the phononic contribution. In the following steps, we calculated magnetic entropy changes in the SBCO_HP2 sample as presented in Figure 5C, which gives 11.3 J mol^{-1}K^{-1}, almost 32% of the theoretically predicted value. It should be noted that the upturn in C_{mag}, as shown in Figure 5C, at low temperatures suggests the suppression of the second magnetic transition under the effect of pressure.

Figure 6A shows the temperature evolution of the dc magnetic susceptibility measured under a magnetic field of 0.1 T for EBCO_HP. The susceptibility increases with decreasing temperature

without any signature of magnetic anomaly, indicating the paramagnetic behavior of this compound. This behavior is supported by the heat capacity data, which exhibits no anomalies in the temperature range of 2–100 K, as displayed in Figure 6B. Generally, for Eu^{3+}-containing compounds, Eu^{3+} ions do not contribute to the magnetism and typically $\mu_{eff}(Eu^{3+}) = 0$. It is expected, therefore, that the ground state for Eu^{3+} may be non-magnetic. At low temperatures, $\chi(T)$ displays Van Vleck paramagnetism which is characteristic of Eu^{3+} compounds and is a result of the sole population of the non-magnetic ground state. As the temperature rises, crystal field states originating from the first excited multiplet are populated. This leads to a temperature-dependent contribution to magnetic susceptibility. Therefore, we have fitted the paramagnetic region by the Curie-Weiss law with an additional Van Vleck contribution, and the fit is presented in the inset of Figure 6A. The fit to the experimental data gives $\mu_{eff} = 6.23\ \mu_B$ and $\theta_{CW} = -140.1$ K. The negative and high value of θ_{CW} indicates the presence of strong antiferromagnetic interaction at low temperatures. Further, as shown in the inset of Figure 6B, there was a finite heat capacity at very low temperatures. Hence, we calculated the lattice contribution from the total heat capacity using the Debye-Einstein model to extract the magnetic entropy associated with it. Figure 6C represents the temperature variation of the magnetic heat capacity, and its inset shows the change in magnetic entropy. The magnetic entropy saturates at a value of 1.1 J mol^{-1}K^{-1}, which is only 3% of the theoretical value for $R[ln(S_{Eu}+1)^2(S_{Cu}+1)] = 38.1$ J mol^{-1}.K^{-1} for $S_{Eu} = 3$ and $S_{Cu} = \frac{1}{2}$ spins. Hence, the compound has a small finite magnetic entropy, indicating the presence of strong short-range correlations and high magnetic frustration.

To investigate further the magnetic properties of this material, magnetic field dependence studies were performed. Figure 7A shows the field dependence at various temperatures for positive and negative fields up to 7 T. Interestingly, the magnetization curve recorded at 2 K shows a nonlinear behavior with a maximum magnetization of 1.5 μ_B/f.u at 7 T. This saturation decreases with an increase in temperature as the paramagnetic contribution becomes more prominent. Such behavior is possible because of the increased magnetic interactions between the Cu^{2+} and/or Eu^{3+}
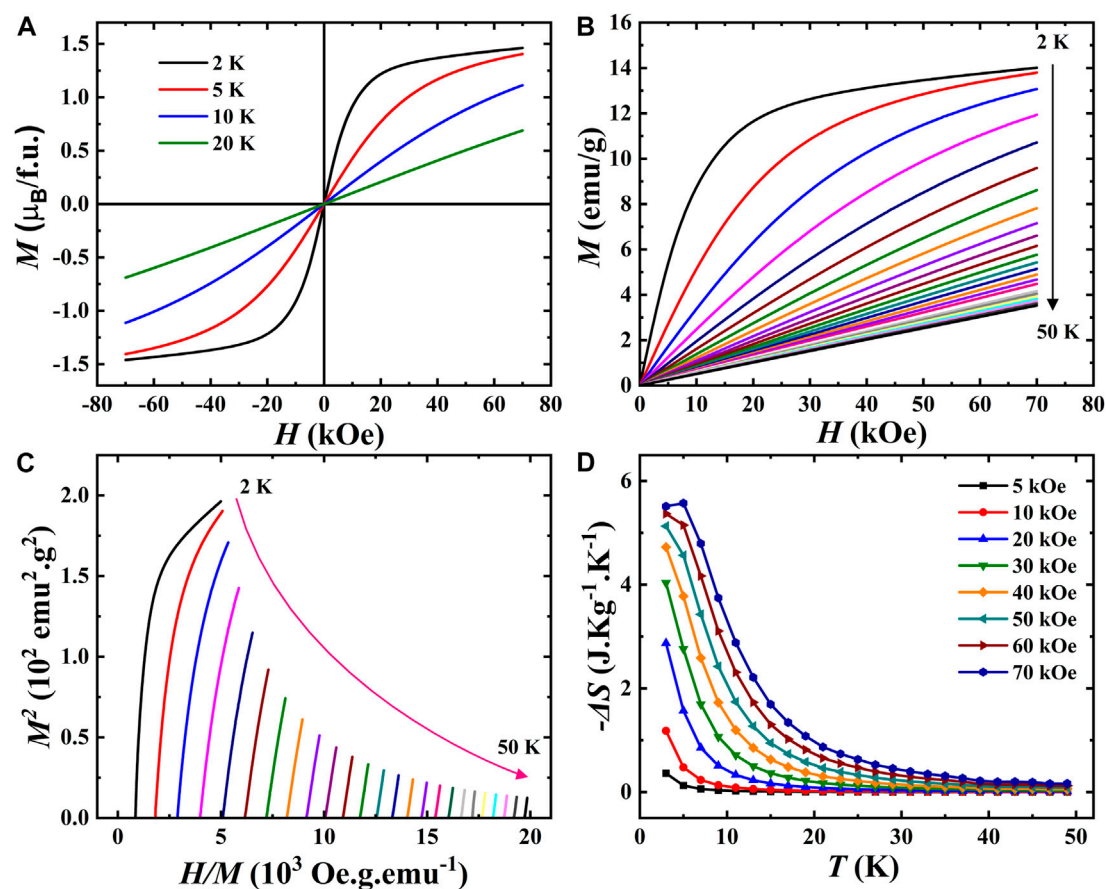
FIGURE 7
(A). Isothermal magnetization against the magnetic field recorded at different temperatures for EBCO_HP. **(B)**. M(H) curves from 2−50 K measured from 0 to 7 T. **(C)**. Arrott plots. **(D)**. Temperature-dependent magnetic entropy change (ΔS) under different magnetic fields obtained from M vs. H data.

spins with temperature lowering. Considering the weak magnetic interaction between the Cu^{2+} and/or Eu^{3+} spins, we now concentrate on the temperature dependence of field-induced saturation and the associated entropy changes in the low-temperature region. Hence, we have explored the magnetocaloric effect (MCE) in this compound and calculated the respective entropy changes during isothermal magnetization processes under the influence of magnetic fields. For this purpose, we have measured single quadrant magnetic-field-dependent isotherms from 2 to 50 K with a temperature interval of 2 K, as depicted in Figure 7B. Arrott plots (M^2 vs. H/M plots) have been used to determine the nature of the magnetic transition, which are shown in Figure 7C. According to Banerjee criterion (Banerjee, 1964), a magnetic phase transition can be first order when the slope of the Arrott curves is negative. In contrast, it will be second-order when the slope is positive. As can be seen from the figure, the slope of the Arrott plots at all the temperatures (except at 2 K) is positive, indicating that the EBCO_HP compound undergoes a second-order magnetic phase transition.

According to classical thermodynamic theory, the change in magnetic entropy (ΔS) produced by the variation of a magnetic field from 0 to H is calculated using the following equation:

$$\Delta S(T, H) = \int_0^H \left(\frac{\partial M}{\partial T}\right)_H dH \qquad (2)$$

The entropy variation as a function of temperature under different magnetic fields is represented in Figure 7D as a function of temperature. The magnetic entropy decreases with increasing temperature, similar to the magnetic susceptibility variation in Figure 7B. We have found that the maximum change in entropy corresponding to a magnetic field variation of 70 kOe at 3 K is about 5.6 J kg^{-1}K^{-1}. Overall, these results indicate Eu_2BaCuO_5 in the tetragonal phase is a good candidate for magnetocaloric materials. Therefore, the different magnetic behaviors of R_2BaCuO_5 (R = rare-earth cations) can be explained based on the Cu-O-R-O-Cu interaction pathway, which apparently can control magnetic interactions.

4 Conclusion

We have successfully synthesized the HP-HT polymorph of the orthorhombic R_2BaCuO_5 (R = Sm and Eu) and studied their structural and magnetic properties. In summary, we can say that "A new form is born" under HP-HT. It is clear from the above

investigations that R_2BaCuO_5 (R = Sm and Eu) exhibits polymorphism under pressure. These materials undergo an irreversible structural phase transition from orthorhombic (SG: $Pnma$) to tetragonal (SG: $P4/mbm$) by an abrupt change in unit cell volume under pressure, in the range 0–1 GPa for Sm-sample based on the pressure-dependent EDXRD studies. The most striking difference between the orthorhombic and tetragonal R_2BaCuO_5 (R = Sm and Eu) structures is the Cu-O coordination environment. In the orthorhombic structure, the Cu atom is coordinated with five oxygen atoms, four of which form the base of a square pyramid. In the tetragonal structure, the Cu atom is tetrahedrally coordinated. It is the first evidence for the existence of tetragonal R_2BaCuO_5 with R = Sm and Eu and extends the well-known tetragonal phase for large rare-earth cations. Also, the discovered new HP-HT polymorph of the orthorhombic R_2BaCuO_5 (R = Sm and Eu) demonstrates the potential of high-pressure synthesis to access novel materials. Further, SBCO_HP1 and SBCO_HP2 samples exhibit antiferromagnetic interactions, while EBCO_HP shows correlated paramagnetic behavior.

Data availability statement

The original contributions presented in the study are included in the article/Supplementary Material, further inquiries can be directed to the corresponding author.

Author contributions

SM: conceptualization, synthesis, data curation, software visualization, formal analysis, writing-original draft. PY: conceptualization. SB: synthesis, data curation. ME: data curation. AS: project administration, supervision, conceptualization, reviewing, writing-reviewing and editing, funding acquisition. All authors contributed to the article and approved the submitted version.

Conflict of interest

The authors declare that the research was conducted in the absence of any commercial or financial relationships that could be construed as a potential conflict of interest.

Publisher's note

All claims expressed in this article are solely those of the authors and do not necessarily represent those of their affiliated organizations, or those of the publisher, the editors and the reviewers. Any product that may be evaluated in this article, or claim that may be made by its manufacturer, is not guaranteed or endorsed by the publisher.

Supplementary material

The Supplementary Material for this article can be found online at: https://www.frontiersin.org/articles/10.3389/fchem.2023.1166475/full#supplementary-material

References

Amador, J., Gutiérrez-Puebla, E., Monge, M. A., Rasines, I., Ruz-Valero, C., Fernandez, F., et al. (1990). Evidence of low-dimensional antiferromagnetic ordering and crystal structure in the R_2BaNiO_5 (R=Y,Er) oxides. *Phys. Rev. B* 42 (13), 7918–7924. doi:10.1103/PhysRevB.42.7918

Andrés, A. De, S. Taboada, Martínez, J. L. A. Salinas, J. Hernández, and Sáez-Puche, R. (1993). Optical phonons in R_2BaMO_5 oxides with M=Co, Ni, Cu, and R=a rare earth. *Phys. Rev. B* 47 (22), 14898–14904. doi:10.1103/PhysRevB.47.14898

Banerjee, B. K. (1964). On a generalised approach to first and second order magnetic transitions. *Phys. Lett.* 12 (1), 16–17. doi:10.1016/0031-9163(64)91158-8

Chattopadhyay, T., J BrownKöbler, P. U., and Wilhelm, M. (1989). Evidence for the antiferromagnetic ordering of the green phase Y_2BaCuO_5. *Europhys. Lett. (EPL)* 8 (7), 685–689. doi:10.1209/0295-5075/8/7/018

Dippel, Ann Christin, Liermann, Hanns Peter, Walter, Peter, Schulte-Schrepping, Horst, Seeck, Oliver H., and Franz, Hermann (2015). Beamline P02.1 at PETRA III for high-resolution and high-energy powder diffraction. *J. Synchrotron Radiat.* 22, 675–687. doi:10.1107/S1600577515002222

Farla, Robert, Bhat, Shrikant, Sonntag, Stefan, Chanyshev, Artem, Ma, Shuailing, Ishii, Takayuki, et al. (2022). Extreme conditions research using the large-volume press at the P61B endstation, PETRA III. *J. Synchrotron Radiat.* 29, 409–423. doi:10.1107/S1600577522001047

García-Matres, E., Martínez, J. L., Rodríguez-Carvajal, J., Alonso, J. A., Salinas-Sánchez, A., and Sáez-Puche, R. (1993a). Structural characterization and polymorphism of R_2BaNiO_5 (R = Nd, Gd, Dy, Y, Ho, Er, Tm, Yb) studied by neutron diffraction. *J. Solid State Chem.* 103 (2), 322–333. doi:10.1006/jssc.1993.1107

García-Matres, E., Rodríguez-Carvajal, J., Martinez, J. L., Alonso, J. A., Salinas-Sánchez, A., and Sáez-Puche, R. (1993b). Polymorphism in the oxides R_2BaNiO_5 (R=Tm, Yb, Lu). *Solid State Ionics* 63 (65), 915–921. doi:10.1016/0167-2738(93)90215-O

Hernández-Velasco, J., and Sáez-Puche, R. (1993). Dimorphism and magnetic properties of Dy_2BaCoO_5. *J. Alloys Compd.* 198 (1–2), 63–67. doi:10.1016/0925-8388(93)90146-E

Hernández-Velasco, J., Salinas-Sánchez, A., and Sáez-Puche, R. (1994). Antiferromagnetic ordering and structural characterization of the Brown colored R_2BaCoO_5 oxides (R = rare earth). *J. Solid State Chem.* 110 (2), 321–329. doi:10.1006/jssc.1994.1175

Indra, A., Mukherjee, S., Majumdar, S., Gutowski, O., Zimmermann, M. V., and Giri, S. (2019). High-temperature ferroelectric order and magnetoelectric coupling driven by the magnetic field cooling effect in R_2BaCuO_5 (R=Er,Dy,Sm). *Phys. Rev. B* 100 (1), 14413. doi:10.1103/PhysRevB.100.014413

Ishii, Yuto, Chen, Jie, Yoshida, Hiroyuki K., Oda, Migaku, Christianson, Andrew D., and Yamaura, Kazunari (2020). High-pressure synthesis, crystal structure, and

magnetic properties of the shastry-sutherland-lattice oxides $BaLn_2ZnO_5$ (Ln = Pr, Sm, Eu). *J. Solid State Chem.* 289, 121489. doi:10.1016/j.jssc.2020.121489

Levitin, R. Z., Mill, B. V., Moshchalkov, V. V., Samarin, N. A., Snegirev, V. V., and Zoubkova, J. (1990). Two magnetic transitions and metamagnetism in the R_2BaCuO_5 (R = Sm, Eu, Gd, Dy, Ho, Er, Tm, Yb) compounds. *J. Magnetism Magnetic Mater.* 90 (91), 536–540. doi:10.1016/S0304-8853(10)80196-9

Mevs, H., and Müller-Buschbaum, H. K. (1989b). Neue oxometallate vom $BaCuSm_2O_6$-typ: $BaCoHo_2O_5$, $BaCoYb_2O_5$ und vom $BaNiLn_2O_5$-typ: $BaCoEr_2O_5$. *Z. Für Anorg. Und Allg. Chem.* 574 (1), 172–176. doi:10.1002/zaac.655740119

Mevs, H., and Müller-Buschbaum, H. K. (1989a). Ein wechsel des strukturtyps in den oxiden $BaCoGd_2O_5$, $BaCoDy_2O_5$ und $BaCoY_2O_5$. *ZAAC - J. Inorg. General Chem.* 573 (1), 128–132. doi:10.1002/zaac.19895730113

Michel, C., and Raveau, B. (1982). Les oxydes A_2BaCuO_5 (A = Y, Sm, Eu, Gd, Dy, Ho, Er, Yb). *J. Solid State Chem.* 43 (1), 73–80. doi:10.1016/0022-4596(82)90216-X

Michel, C., and Raveau, B. (1983). Ln_2BaZnO_5 and $Ln_2BaZn_{1-x}Cu_xO_5$: A series of zinc oxides with zinc in a pyramidal coordination. *J. Solid State Chem.* 49 (2), 150–156. doi:10.1016/0022-4596(83)90108-1

Müller-Buschbaum, H. K., and Sonne, P. (1990). $BaZnNd_2O_5$: Eine neue struktur bei oxometallaten $BaMLn_2O_5$. *J. Less-Common Metals* 167 (1), 193–198. doi:10.1016/0022-5088(90)90305-4

Puche, R. Sáez, E., Fernández-Díaz, M. T., and Cascales, C. (2008). Magnetic characterization of Pr_2BaCuO_5. *J. Phys. Condens. Matter* 20 (4), 045210. doi:10.1088/0953-8984/20/04/045210

Rodríguez-Carvajal, J. (1993). Recent advances in magnetic structure determination by neutron powder diffraction. *Phys. B Phys. Condens. Matter* 192 (1–2), 55–69. doi:10.1016/0921-4526(93)90108-I

Sáez Puche, R., Climent, E., Jiménez-Melero, E., Romero De Paz, J., Martínez, J. L., and Fernández-Díaz, M. T. (2006). Neutron powder diffraction study on Nd_2BaCuO_5 oxide. *J. Alloys Compd.* 408 (412), 613–617. doi:10.1016/j.jallcom.2004.12.060

Sáez-Puche, R., Coronado, J. M., Martín-Llorente, J. M., and Rasines, I. (1992). Antiferromagnetism in the R_2BaNiO_5 oxides (R = Nd, Eu, Dy, Ho). *Mater. Chem. Phys.* 31 (1–2), 151–154. doi:10.1016/0254-0584(92)90168-8

Sáez-Puche, R., and Hernández-Velasco, J. (1994). Structural relationships and magnetic behaviour in R_2BaMO_5 oxides (R = rare earth; M = Co, Ni and Cu). *Adv. Mater. Res.* 1 (2), 65–82. doi:10.4028/www.scientific.net/amr.1-2.65

Sáez-Puche, R., Herrera, S. R., and Martínez, J. L. (1998). Synthesis and magnetic behaviour of the novel Pr_2BaCuO_5 oxide. *J. Alloys Compd.* 269 (1–2), 57–59. doi:10.1016/S0925-8388(98)00163-7

Salinas-Sánchez, A., García-Muñoz, J. L., Rodríguez-Carvajal, J., Sáez-Puche, R., and Martinez, J. L. (1992). Structural characterization of R_2BaCuO_5 (R = Y, Lu, Yb, Tm, Er, Ho, Dy, Gd, Eu and Sm) oxides by X-ray and neutron diffraction. *J. Solid State Chem.* 100 (2), 201–211. doi:10.1016/0022-4596(92)90094-C

Salinas-Sánchez, A., Sáez-Puche, R., and Alario-Franco, M. A. (1990). Evidence of antiferromagnetic order in the green phases R_2BaCuO_5 (R = Dy, Y, and Yb). *J. Solid State Chem.* 89 (2), 361–365. doi:10.1016/0022-4596(90)90277-5

Salinas-Sánchez, A., Sáez-Puche, R., Rodríguez-Carvajal, J., and Martínez, J. L. (1991). Structural characterization of R_2BaNiO_5 (R=Tm and Yb): Polymorphism for R=Tm. *Solid State Commun.* 78 (6), 481–488. doi:10.1016/0038-1098(91)90361-X

Salinas-Sánchez, A., and Sáez-Puche, R. (1993). Structural characterization and magnetic properties of $LaRBaCuO_5$ oxides (R=rare earth). *Solid State Ionics* 63–65 (8), 927–931. doi:10.1016/0167-2738(93)90217-Q

Schiffler, St., and Müller-Buschaum, H. K. (1986a). Ein neuer strukturtyp zur formel $ABLn_2O_5$ zur kenntnis von $BaNiNd_2O_5$. *Z. Für Anorg. Und Allg. Chem.* 532 (1), 10–16. doi:10.1002/zaac.19865320103

Schiffler, St., and Müller-Buschbaum, H. K. (1987a). Neue verbindungen zum $BaNiNd_2O_5$-typ: $BaNiLn_2O_5$ (Ln=Sm, Gd, Ho, Er, Tm). *Monatsh. Für Chem. Chem. Mon.* 118 (6–7), 741–747. doi:10.1007/BF00809224

Schiffler, St., and Müller-Buschbaum, H. K. (1987b). Neue verbindungen zum $BaPtNd_2O_5$-typ: $BaMLn_2O_5$ (M = Pt, ln ≡ Sm, Gd; M = Pd, ln = Pr, Tb). *J. Less Common Metals* 128 (February), 117–123. doi:10.1016/0022-5088(87)90197-4

Schiffler, St., and Müller-Buschbaum, H. K. (1986b). $BaNiYb_2O_5$ – eine verbindung, die nicht im $BaNiLn_2O_5$-typ kristallisiert mit einem beitrag über $BaCuSm_2O_5$. *Z. Für Anorg. Und Allg. Chem.* 540 (9–10), 243–250. doi:10.1002/zaac.19865400927

Seto, Yusuke, Nishio-Hamane, Daisuke, Nagai, Takaya, and Sata, Nagayoshi (2010). Development of a software suite on X-ray diffraction experiments. *Rev. High Press. Sci. Technology/Koatsuryoku No Kagaku Gijutsu* 20 (3), 269–276. doi:10.4131/jshpreview.20.269

Seto, Yusuke (2012). Whole pattern fitting for two-dimensional diffraction patterns from polycrystalline materials. *Rev. High Press. Sci. Technol.* 22 (2), 144–152. doi:10.4131/jshpreview.22.144

Yanda, Premakumar (2021). *Magnetoelectric Multiferroic Prop. Green Phases R_2BaCuO_5 Aeschynites RFeWO_6 R= Rare Earth.* http://lib.jncasr.ac.in:8080/jspui/handle/123456789/3229.

Yanda, Premakumar, Golosovsky, I. V., Mirebeau, I., Ter-Oganessian, N. V, Rodríguez-Carvajal, J., and Sundaresan, A. (2020). Interplay of 4f-3d interactions and spin-induced ferroelectricity in the green phase Gd_2BaCuO_5. *Phys. Rev. Res.* 2 (2), 1–7. doi:10.1103/PhysRevResearch.2.023271

Yanda, P., Orlandi, F., Manuel, P., Boudjada, N., Rodriguez-Carvajal, J., and Sundaresan, A. (2021). Magnetic-field-induced ferroelectric states in centrosymmetric R_2BaCuO_5 (R = Dy and Ho). *Phys. Rev. B* 104 (14), 144401. doi:10.1103/PhysRevB.104.144401

Yanda, Premakumar, Ter-Oganessian, N. V., and Sundaresan, A. (2019). Linear magnetoelectric effect in antiferromagnetic Sm_2BaCuO_5. *Phys. Rev. B* 100 (10), 104417. doi:10.1103/PhysRevB.100.104417